HHS Public Access

Author manuscript

IEEE Trans Med Imaging. Author manuscript; available in PMC 2018 June 01.

Published in final edited form as:

IEEE Trans Med Imaging. 2017 June ; 36(6): 1297–1305. doi:10.1109/TMI.2017.2664799.

Multi-Modality Imaging Enables Detailed Hemodynamic Simulations in Dissecting Aneurysms in Mice

Evan H. Phillips[†],
Weldon School of Biomedical Engineering, Purdue University, West Lafayette, IN, 47907, USA

Paolo Di Achille[†],
Department of Biomedical Engineering, Yale University, New Haven, CT, 06520, USA. He is now with IBM Research, Yorktown Heights, NY, 10598, USA

Matthew R. Bersi[†],
Department of Biomedical Engineering, Yale University, New Haven, CT, 06520, USA. He is now with the Department of Biomedical Engineering, Vanderbilt University, Nashville, TN, 37212, USA

Jay D. Humphrey, and
Department of Biomedical Engineering and Vascular Biology and Therapeutics Program, Yale University, New Haven, CT, 06520, USA

Craig J. Goergen
Weldon School of Biomedical Engineering, Purdue University, West Lafayette, IN, 47907, USA

Abstract

A multi-modality imaging based modeling approach was used to study complex unsteady hemodynamics and lesion growth in a dissecting abdominal aortic aneurysm model. We combined in vivo ultrasound (geometry and flow) and in vitro optical coherence tomography (geometry) to obtain the high resolution needed to construct detailed hemodynamic simulations over large portions of the murine vasculature, which include fine geometric complexities. We illustrate this approach for a spectrum of dissecting abdominal aortic aneurysms induced in male apolipoprotein E-null mice by high-dose angiotensin II infusion. In vivo morphological and hemodynamic data provide information on volumetric lesion growth and changes in blood flow dynamics, respectively, occurring from the day of initial aortic expansion. We validated the associated computational models by comparing results on time-varying outlet flows and vortical structures within the lesions. Three out of four lesions exhibited abrupt formation of thrombus, though different in size. We determined that a lesion without thrombus formed with a thickened vessel wall, which was resolvable by OCT and histology. We attribute differences in final sizes and compositions of these lesions to the different computed flow and vortical structures we obtained in our mouse-specific fluid dynamic models. Differences in morphology and hemodynamics play crucial roles in determining the evolution of dissecting abdominal aortic aneurysms. Coupled high-resolution in vivo and in vitro imaging approaches provide much-improved geometric models for

Correspondence to: Craig J. Goergen.

[†]indicates equal contribution

hemodynamic simulations. Our imaging-based computational findings suggest a link between perturbations in hemodynamic metrics and aneurysmal disease heterogeneity.

Index Terms

Aneurysm; Aortic Dissection; Animal models and imaging; Ultrasound; Optical Imaging; Optical Coherence Tomography (OCT); DOT; Multi-modality fusion; Hemodynamics; Computational fluid dynamic models; Quantification and estimation; Blood Vessels

I. INTRODUCTION

THE increasing availability of genetically altered, pharmacologically treated, and surgically modified mice has rendered the mouse the animal model of choice in many studies of vascular biology and mechanics. As an illustrative example, chronic infusion of angiotensin II (AngII) in male apolipoprotein E-null (*ApoE*$^{-/-}$) mice yields a reproducible model of dissecting aortic aneurysm, often including a false lumen with intramural thrombosis [1, 2]. Given that hemodynamics is critical to the formation and growth of aneurysms, dissections, and thrombus [3–5], there is strong motivation to develop sophisticated data-driven models of the associated changes in blood flow, pressure, and wall mechanics. Yet, the small dimensions of the murine vasculature combined with the high heart rate present significant experimental challenges, both in vivo and in vitro.

The purpose of the present study is to implement a multi-modality imaging based modeling approach to investigate the heterogeneity of blood flow dynamics and growth in the AngII model. We show that a combination of in vivo data from high-frequency ultrasound (US), quantifying geometry and blood flow, with in vitro data from optical coherence tomography (OCT), quantifying fine geometry within the lesion, enables sophisticated three-dimensional computational models suitable for detailed studies of the hemodynamics in the AngII infusion model. As representative examples, we present US-OCT-based models and simulations of the suprarenal abdominal aorta (SAA) for one mouse representing a modest dilation of the wall, with no visible thrombus, as well as for three mice representing progressively severe dissecting aneurysms having different sized false lumens and varying degrees of intramural thrombus. It is shown that hemodynamic simulations over a cardiac cycle can be tuned to capture well the flow profiles in the associated outlet vessels (infrarenal aorta, renal arteries, celiac artery, and superior mesenteric artery), thus increasing confidence in the simulations for other regions, including the false lumen. Qualitative comparisons of measured and computed flows within the lesions further demonstrate the goodness of the mouse-specific models. We submit that this multi-modality imaging approach can offer considerable advantages for informing hemodynamic simulations of complex conditions in the murine vasculature.

II. MATERIALS AND METHODS

Detailed materials and methods as well as supplemental figures and movies are provided in the supplementary files/multimedia tab. We received approval from the Institutional Animal Care and Use Committee to conduct all animal procedures. Briefly, mini-osmotic pumps

were implanted surgically in male *ApoE*$^{-/-}$ mice to deliver AngII at 1000 ng/kg/min for up to 28 days. The SAA was monitored every 48 hours post-operatively using US to detect the initiation of a dissecting aneurysm, after which lesion geometry and blood flow were quantified using a battery of US imaging modalities (B-mode, M-mode, pulsed wave (PW) Doppler, and ECG-gated kilohertz visualization (EKV) mode) every two days for seven days. Diastolic and systolic arterial blood pressures were measured in conscious mice, using a tail-cuff device, at baseline, on days 3 and 7 post-surgery, and on day 4 post-diagnosis of a lesion. The abdominal aorta including the lesion was harvested at 7 days and the in vivo configuration was re-established in vitro to enable OCT quantification of fine details within the region of the dissected aneurysm. Datasets from the two imaging modalities were co-registered using the "Transforms" module of the 3D Slicer open-source software (NA-MIC; https://www.slicer.org/). Following imaging, specimens were fixed and prepared for standard histological examination.

Using the combined US-OCT data, computational models of the hemodynamics were built to study detailed patterns of blood flow in and near the dissected region. Fig. 1 shows how a typical domain reconstruction provides significant detail on the morphology of regions in and near the dissected aneurysm (red), including the false lumen and thrombus (blue).

The inlet flow for the hemodynamic simulation was prescribed using US data whereas outlet boundary conditions were determined using a data-informed 1D wave propagation model (Supplemental Fig. I). Finally, simulations were validated by comparing computed and measured flows within all major vessels in the suprarenal region (see below).

We assessed statistical significance (paired Student's t-test and two-sample t-test; $\alpha = 0.05$) of select parameters between two times (e.g. baseline and day 7 post-diagnosis) or between lesion and proximal/distal regions. One-way analysis of variance (ANOVA) was used to test differences in mean systolic blood pressure at multiple times post-surgery relative to baseline (Dunnett's test; $\alpha = 0.05$).

III. RESULTS

Of seven mice infused with AngII, one presented with an expanded aortic wall without dissection (mouse M1) whereas three developed dissecting aneurysms of the SAA (mice M2 to M4). We identified these expansions by US on average 7.5±1.7 days (6–9 days) after implanting the mini-osmotic pumps. Below, we focus on results from these four animals (M1 – M4), which represent a natural spectrum of early AngII-induced phenotypes despite all being harvested 7 days following the initial diagnosis (i.e., ~ 14.5 days post-surgery).

A. Dissection results in rapid changes in geometry

The initial dissection event was responsible for much of the localized enlargement experienced by the aorta (Fig. 2). Effective maximum diameter increased 57 ± 9% (n=4), from 1.19 ± 0.11 mm at baseline (day −1) to 1.87 ± 0.24 mm on the day of diagnosis (day 0), which was significantly different (p<0.01). Likewise, total volume increased significantly during this first day (from 7.65 ± 2.05 mm^3 on day −1 to 19.73 ± 3.54 mm^3 on day 0;

p<0.01), but much less so (a further 26 ± 9%) over the subsequent week (from day 0 to 7) for those mice with marked lesions, namely M2 to M4.

Evolving effective maximum diameter nevertheless correlated well with evolving total volume and thrombus volume from day 0 to day 7 (Supplemental Fig. II). Lesions in mice M2 to M4 also exhibited a loss of true lumen volume from baseline to day 0 (−52 ± 28%, or a total of 4.01 ± 1.66 mm^3). Although this initial reduction did not reach statistical significance (p=0.2), it was partially offset within one day by a volumetric increase of 38 ± 22%, perhaps due to retraction or compaction of the thrombus. Indeed, by day 7 the true lumen volume had recovered up to 70 ± 23% of its original (pre-dissection) value. Although all mice presented with some enlargement of the SAA proximal to the celiac branch, M1 did not show any luminal reduction, signs of intramural delamination, or thrombus formation. Instead, the true lumen volume increased by 25% at day 0 and 51% by day 7, while the total lesion volume increased only negligibly (< 1%) after initial expansion but without developing an aneurysmal shape.

B. Dissections increase aortic stiffness and alter hemodynamics, leading to acute but evolving thrombus

Consistent with morphologic assessments, PW Doppler measurements revealed marked differences in blood flow before and after the dissection (Fig. 3). Mice presenting with a dissection-related false lumen and thrombus (M2 to M4) exhibited a significant initial increase in blood flow velocity at the site just proximal to the intimal opening into the dissection (172 ± 12% increase in mean velocity from baseline to day 0), which appeared to result from the reduction in the true lumen in that region (cf. Fig. 2). Such increases reduced partially (to 49 ± 8%) over the subsequent week, consistent with the partial recovery in true lumen volume. Intramural thrombus had variable sizes and growth depending on the lesion analyzed, but it constituted at least 66 ± 13% of the total volume during the first week (Fig. 2; Supplemental Movie I). Only for the largest lesion (M4) did the outer wall of the lesion appreciably expand as the thrombus grew in volume. Serial US scans of M4 show an increase in thrombus deposition and complex flow patterns after day 0 (Supplemental Movie II). M1 showed a different behavior, with a decrease in mean velocity (−46%) soon after detecting a modest focal widening of the SAA that did not lead to intramural thrombus. This reduction persisted through the first week of development. Color Doppler Data also provided important qualitative information on the flow dynamics, such as the presence or absence of recirculating flow. For example, we identified recirculating flow in the false lumen of M3 using Color Doppler (Supplemental Movie III).

In vivo structural stiffness, evaluated by M-mode US, showed a consistent tendency across the four mice (Fig. 3 c–d). Cyclic circumferential strain in the middle of the aneurysms for animals M2 to M4 decreased significantly (83 ± 24% reduction; p<0.05) from 16 ± 4.6% to 2.7 ± 0.8% soon after dissection and remained reduced (40 ± 9% reduction between days 0 and 7). Cyclic circumferential strain in the same region, SAA, of M1 also dropped sharply on day 0 (80% reduction) and remained reduced. Supplementary materials are available in the supplementary files/multimedia tab.

C. Multi-modality reconstructions compare well with histology

Dissected aneurysms present complex morphologies, with regions of blood flow within the false lumen delineated from regions filled with thrombus and bounded by non-uniformly thickened aortic walls. The resolution offered by 3D US alone often did not provide sufficient detail to capture such complexities, which would prevent suitable reconstructions of the domains needed for detailed hemodynamics simulations.

Combining in vivo 3D US with in vitro OCT imaging enabled detection of the main morphologic transitions characterizing each lesion, which differed markedly in terms of total false lumen volume as well as by regions of free-flowing blood versus thrombus. After reconstructing the four geometries, we compared our segmentations qualitatively to histological images for the same specimen taken at three different locations to assess morphology as a function of axial position. Notwithstanding ubiquitous shrinkage and distortion of cross-sections in histological images, Fig. 4 shows that our segmentations agreed qualitatively with histology for all four vessels (M1 to M4), including regions without dissection, dissections with false lumens, and dissections with merged lumens. Most importantly, regions with thrombus were captured well by the OCT imaging.

D. Advantages of 3D US-OCT

Segmentation of 3D US images allows one to delineate major features of a dissection (cf. Figs. 1 and 4), including total volume and true lumen volume [6] and to coarsely differentiate wall, thrombus, and open false lumen. Enriching the US images with information provided by the OCT images, with a 7 μm spatial resolution, improved our overall segmentation markedly, particularly when discerning different regions composing the intramural cavity. Table I compares measurements obtained using 3D US images acquired at day 7 (segmentation performed using Vevo LAB software) with results obtained using our combined US+OCT approach (segmentation performed using the code *SimVascular* after co-registration and processing of the images). We normalized these results by the length of the considered volumes because measurements taken using the combined approach were typically limited to shorter samples due to the tissue cannulation required by the mechanical testing informed OCT imaging.

Discrepancies between the two methods were modest but not negligible for assessments of true lumen volume (average normalized error of 8.1 ± 2.0%), dissection region (12.6 ± 15.2%), and total lesion (7.7 ± 5.3%). Differences were much more pronounced, however, for measurements delineating regions within the intramural cavity (i.e., false lumen and thrombus). As expected, relative differences between volume measurements inferred using 3D US and OCT techniques were small, with only two exceptions that fell outside the 95% confidence intervals (Supplemental Fig. III). While 3D US provides reliable estimates of lesion volume, more than volume is needed for a clear description of these complex pathologies (i.e., false lumen geometry). Thus, the increased resolution of the combined US-OCT approach allowed us to demarcate better the false lumen boundaries, even allowing detection of a small (0.08 mm^3) volume for M2 that was not visible on 3D US images but was evident with histology. This demarcation is in contrast to previous studies that have used

US alone and have not been able to delineate the composition of the aortic wall or the inner and outer aortic diameters [7].

E. Hemodynamic simulations agree well with measurements

Combining high-resolution OCT data of the dissection and nearby vasculature morphology with time-averaged Doppler US data of the inlet and outlet flows through all relevant major branches within the abdominal aorta resulted in improved mouse-specific models of the hemodynamics. Table II shows prescribed mouse-specific inlet flow rates and optimal values for resistance and capacitance (determined using the 1D wave propagation model; cf. Supplemental Fig. I) used as boundary conditions for the hemodynamic simulations.

We then compared velocity waveforms measured using PW Doppler (cf. Fig. 3) with those predicted by our 3D simulations (Fig. 5). While the inlet boundary condition was prescribed at the proximal aorta, the outlet conditions at the celiac, superior mesenteric, right renal, and left renal branches were optimized using the aforementioned 1D wave propagation model to match the US measurements (i.e., good agreement was expected). To evaluate further the quality of the simulations, we also compared velocity waveforms proximal to the dissection that were not used to inform the simulations; agreement was always strong. For visual purposes, we show 3D renderings of the velocity magnitude at systole and diastole for all four mice in Fig. 5. Overall, M1 and M3 showed the best and worst agreements with measured data, respectively, but results at all locations were reasonable. Goodness of fit values evaluated as correlation coefficients between predicted and measured waveforms ranged between 0.86 at the celiac branch of M2 to 0.98 for M3 proximally to the lesion. The average correlation coefficient at all of the probed locations was 0.94 ± 0.04.

F. 3D US-OCT based simulations of false lumen flow

Suprarenal abdominal aortic dissections are known to differ morphologically in terms of lesion size, extent of thrombosis, and overall spatial enlargement even when evaluated at similar times of AngII infusion [8]. Rather than base our study on the days post-surgery, we screened mice for initial aortic expansion and focused on a fixed short-term period after the initial diagnosis (7 days). Our combined 3D US-OCT approach allowed us to capture lesion-to-lesion differences with high spatial detail (Supplemental Fig. III) and to visualize and model complex hemodynamics (Fig. 6; Supplemental Movies I and III). Table III lists general characteristic features of the four lesions, ordered based on the Daugherty classification (Type I, II, or III lesion) and the presence and size of a false lumen [2]. The last group of rows provides average hemodynamic indices and changes in blood flow velocity predicted by the hemodynamic simulations. The very low values of time-averaged wall shear stress (TAWSS) in the false lumen ($82 \pm 12\%$ lower than in healthy segments of the SAA) indicate significantly perturbed hemodynamics.

Fig. 6 shows the evolution over a cardiac cycle of color-coded vortical (λ_2) distributions on longitudinal cross-sections for the four lesions, M1 to M4. Shown overlapped are streamlines seeded from points lying on the false lumen orifice area or, for M1, immediately proximal to the dilatation. λ_2 is defined as the second largest eigenvalue of the tensor

$$s^2+\Omega^2$$

where $\boldsymbol{S}$ and $\boldsymbol{\Omega}$ are, respectively the symmetric and the antisymmetric part of the spatial velocity gradient tensor, $\boldsymbol{L}$, which can be written [9, 10]:

$$\boldsymbol{L}=\partial \boldsymbol{v}/\partial \boldsymbol{x}$$

Regions where λ_2 is negative are of potential interest because they can indicate the presence of vortical flows, which are bounded by regions of high shear and enclose a local pressure maximum. High fluid shear in turn can activate platelets [11].

Most of the vortices in the true lumen occupy a relatively stable position throughout the cardiac cycle. This finding is particularly evident in M1, where no major recirculation event occurs. The presence of a false lumen in M2, M3, and M4 lesions seems to facilitate the formation of vortical structures that persist within the dissection cavity for large parts of the cardiac cycle. While the dynamics, duration, and migration patterns of these vortices seem to vary from case to case, the negative λ_2 regions always form initially close to the proximal end of the false lumen opening. Fig. 6 also shows snapshots of EKV measurements acquired at day 7 post-diagnosis. For qualitative comparison with the simulated results, a digital image correlation based particle tracking algorithm was applied to the EKV images and red arrows indicate directions of blood flow in the imaging plane.

IV. DISCUSSION

Given the increasing usage of mouse models for vascular studies, it is not surprising that many papers now report hemodynamic simulations. Indeed, advances in different imaging modalities – especially high-frequency US, magnetic resonance imaging (MRI), and micro-CT – have enabled investigators to build mouse-specific geometric models for both 1-D and 3-D simulations. For example, Greve et al. [12] used phase-contrast and time-of-flight MRI (4.7 T) to build 3-D models of the hemodynamics within the normal murine infrarenal abdominal aorta and showed that mean wall shear stresses are much higher in the mouse (~8 Pa) than in humans (~0.5 Pa). Resolution was reported to be on the order of 117 μm (i.e., in-plane voxels ~0.0117 cm). Feintuch et al. [13] used a Vevo 770 US system (FUJIFILM VisualSonics), with a stated resolution of ~100 μm (lateral) by ~65 μm (axial), to inform models of the hemodynamics within the murine aortic arch. They further showed a good correspondence between US and MRI measured volumetric flows in the arch and major branches. Huo et al. [14] combined PW Doppler US, to measure mean velocities in the ascending aorta, with both a perivascularly placed flowmeter, to measure flows in the abdominal aorta, and micro-CT images of plastic casts of the entire murine aorta, to extract geometric information. Spatial resolution was not given although the significant figures reported would imply ~10 μm. Plastic casts, injected at 100 mmHg, are yet difficult to make reliably and the reported values for key vessels differ considerably from values reported by others (e.g., left common carotid diameter of ~640 μm versus 490 μm reported by Suo et al. [15] and 460 μm by Trachet et al. [16]). Amirbekian et al. [17] used MRI, with a stated

spatial resolution of ~69 μm × 69 μm, to build computational models of the abdominal aorta, whereas Trachet et al. [16] combined micro-CT with a theoretical resolution of 46 μm, to obtain arterial geometries, and US (Vevo 2100), to obtain information on flows needed to prescribe boundary conditions.

Whereas the aforementioned studies focused on imaging-based models for computing normal hemodynamics, both US [7, 18] and MRI [19–22] have also been used to assess lesion growth or wall strain in the AngII infusion model of dissecting aneurysms. Favreau et al. [7] used high-frequency US alone, which did not allow them to "accurately differentiate between the intraluminal and extraluminal aortic wall." To the best of our knowledge, only Ford et al. [23] have built mouse-specific US imaging-based models of hemodynamics within such lesions. Their study was carried out using a single-element transducer with an equivalent 40 μm axial and 90 μm lateral spatial resolution (RMV704 transducer, Vevo770). They reported spatio-temporal results for TAWSS, oscillatory shear index (OSI), and relative residence time, but focused largely on vorticity. They concluded that "maximum remodeling occurs in the areas where vortical structures are located, which in turn result in the greatest fluctuations in shear stress" (i.e., OSI). They acknowledged, however, that they did not model the separate outlet branches, they did not have subject-specific inlet flow waveforms, and that higher resolution imaging "would have been desirable". Indeed, there was no delineation of freely flowing versus clotted blood in the false lumens. Based on this brief survey, we concluded that prior geometric models of the murine vasculature have been built on data from either in vivo or combined in vivo, in situ, and in vitro imaging with spatial resolutions ranging from ~40 to 120 μm. The spatial resolution of our US system (Vevo2100) is the same as used by Trachet et al. [16] and thus reasonable for modeling the major aortic vessels. We suggest that fine details inherent to a dissecting aneurysm demand increased resolution.

Here we have introduced a combination of moderate resolution (~40 μm) in vivo anatomical and functional US imaging with high resolution (~7 μm) in vitro OCT imaging to build computational models of complex dissecting aneurysms in the suprarenal aorta. We monitored mice noninvasively for initial aortic expansion and obtained early in vivo data of lesion morphology, composition, and hemodynamics. In this way, we were able to construct the first detailed models of flow within the false lumen of a dissected murine suprarenal abdominal aorta for a spectrum of lesions ranging from mild to severe. We confirmed that expansion occurs abruptly in the vicinity of a focal dissection and that growth can be either minimal or gradual over the short term after this initial event. In vitro images were obtained only after reproducing in vivo mechanical loading conditions, namely restoring the axial stretch and imposing a transmural pressure of 80 mmHg. Multi-modality images were co-registered using native fiducial markers and verified qualitatively via comparison with standard histological images; even open versus thrombotic false lumens were delineated and modeled well. The associated computational hemodynamic model was further informed by subject-specific measured inlet flows and optimized RCR-Windkessel outlet parameters that enabled flow waveforms in all of the major outlet vessels to be described reasonably well. After ensuring that flows matched well in a region not used to inform the computational model, we relied on our simulation results to analyze vortical structure behavior throughout the cardiac cycle. Our analyses suggested that a false lumen cavity is necessary for the

formation of major recirculating events and vortices initially form at the proximal end of the false lumen opening.

We note that there were some challenges and limitations in this study. Abdominal gas diminishes US image quality and was occasionally present when imaging. This issue was notable on day 7 at the distal end of the lesion for M4, making detailed US-based segmentation of the open false lumen and thrombus difficult. We overcame this problem by using morphological and compositional image data derived from OCT and histology. In general, US data with minimal artifacts allowed us to delineate regions with free-flowing blood from thrombus; however, the superior resolution of OCT was necessary to confirm and model the detailed composition of the dissected region. There can also be noise in M-mode measurements, which particularly impacts the magnitude of the lowest percent strain values. OCT has limitations in depth of penetration, which can reduce our ability to visualize the thickest arterial walls. Our custom US-OCT co-registration, however, was able to enhance penetration and our ability to discriminate structural features within the lesions. We do not have a secondary imaging comparison (i.e. MRI or micro-CT) of the volume measurements; however, our prior US and MRI imaging studies reveal similar volumetric measurements for other comparable lesions [6, 21, 22]. The volume/length values of the lesions investigated previously fall within a similar range as those presented here (1 to 3 mm^2). The commercially available US system we used in the present study has been validated extensively, suggesting that our volume estimates for total lesion, true lumen, and false lumen are precise. Lastly, the assumption of a rigid wall in the hemodynamic simulations introduces systematic errors, particularly in predicted wall shear stress values. It is well known that rigid wall simulations tend to overestimate wall shear stress magnitude in areas of relatively simple hemodynamics (e.g. pre-aneurysmal SRA) while they underestimate wall shear stress in regions of stagnation (e.g. surface of dissection cavity). We took great care to acquire and inform the model with velocity information at all branching vessels. Therefore, we are confident that our simulations of observed general behavior (vortex formation and development) are reliable, and of great interest for understanding intra-lesion hemodynamics.

In summary, complex vascular lesions in mice, such as dissecting aneurysms that cause abrupt aortic expansion and complex intramural channels, exhibit fine structural heterogeneities that are important when computing the hemodynamics to identify possible causative biomechanical metrics. Notwithstanding advances in US, MRI, and micro-CT, combining in vivo imaging data with high resolution imaging data obtained in vitro using OCT can provide much-improved geometric models for computational simulations. Computational models of the hemodynamics, in turn, are essential for providing information needed to characterize better the relationships between hemodynamics, wall growth and remodeling, and disease progression [5].

Supplementary Material

Refer to Web version on PubMed Central for supplementary material.

Acknowledgments

This work was supported, in part, by grants from the American Heart Association (14SDG18220010 to C.J.G) and NIH (R01 HL086418 to J.D.H and U01 HL116323 to J.D.H and Dr. George Karniadakis).

References

1. Daugherty A, Manning MW, Cassis LA. Angiotensin II promotes atherosclerotic lesions and aneurysms in apolipoprotein E-deficient mice. J Clin Invest. Jun.2000 105:1605–12. [PubMed: 10841519]
2. Daugherty A, Manning MW, Cassis LA. Antagonism of AT2 receptors augments angiotensin II-induced abdominal aortic aneurysms and atherosclerosis. Br J Pharmacol. Oct.2001 134:865–70. [PubMed: 11606327]
3. Dillon-Murphy D, Noorani A, Nordsletten D, Figueroa CA. Multi-modality image-based computational analysis of haemodynamics in aortic dissection. Biomech Model Mechanobiol. Aug. 2016 15:857–76. [PubMed: 26416312]
4. Di Achille P, Tellides G, Figueroa CA, Humphrey JD. A haemodynamic predictor of intraluminal thrombus formation in abdominal aortic aneurysms. Proceedings of the Royal Society A: Mathematical, Physical and Engineering Sciences. 2014; 470
5. Humphrey JD, Taylor CA. Intracranial and abdominal aortic aneurysms: similarities, differences, and need for a new class of computational models. Annu Rev Biomed Eng. 2008; 10:221–46. [PubMed: 18647115]
6. Phillips EH, Yrineo AA, Schroeder HD, Wilson KE, Cheng JX, Goergen CJ. Morphological and Biomechanical Differences in the Elastase and AngII apoE(−/−) Rodent Models of Abdominal Aortic Aneurysms. Biomed Res Int. 2015; 2015:413189. [PubMed: 26064906]
7. Favreau JT, Nguyen BT, Gao I, Yu P, Tao M, Schneiderman J, et al. Murine ultrasound imaging for circumferential strain analyses in the angiotensin II abdominal aortic aneurysm model. J Vasc Surg. Aug.2012 56:462–9. [PubMed: 22503226]
8. Manning MW, Cassi LA, Huang J, Szilvassy SJ, Daugherty A. Abdominal aortic aneurysms: fresh insights from a novel animal model of the disease. Vasc Med. Feb.2002 7:45–54. [PubMed: 12083734]
9. Jeong J, Hussain F. On the identification of a vortex. J Fluid Mech. 1995; 285:69–94.
10. Biasetti J, Hussain F, Gasser T. Blood flow and coherent vortices in the normal and aneurysmatic aortas: a fluid dynamical approach to intra-luminal thrombus formation. J R Soc Interface. 2011; 8:1449–61. [PubMed: 21471188]
11. Di Achille P, Tellides G, Humphrey JD. Hemodynamics-Driven Deposition of Intraluminal Thrombus in Abdominal Aortic Aneurysms. Int J Numer Method Biomed Eng. Aug 29.2016
12. Greve JM, Les AS, Tang BT, Draney Blomme MT, Wilson NM, Dalman RL, et al. Allometric scaling of wall shear stress from mice to humans: quantification using cine phase-contrast MRI and computational fluid dynamics. Am J Physiol Heart Circ Physiol. Oct.2006 291:H1700–8. [PubMed: 16714362]
13. Feintuch A, Ruengsakulrach P, Lin A, Zhang J, Zhou YQ, Bishop J, et al. Hemodynamics in the mouse aortic arch as assessed by MRI, ultrasound, and numerical modeling. Am J Physiol Heart Circ Physiol. Feb.2007 292:H884–92. [PubMed: 17012350]
14. Huo Y, Guo X, Kassab GS. The flow field along the entire length of mouse aorta and primary branches. Ann Biomed Eng. May.2008 36:685–99. [PubMed: 18299987]
15. Suo J, Ferrara DE, Sorescu D, Guldberg RE, Taylor WR, Giddens DP. Hemodynamic shear stresses in mouse aortas: implications for atherogenesis. Arterioscler Thromb Vasc Biol. Feb.2007 27:346–51. [PubMed: 17122449]
16. Trachet B, Renard M, De Santis G, Staelens S, De Backer J, Antiga L, et al. An integrated framework to quantitatively link mouse-specific hemodynamics to aneurysm formation in angiotensin II-infused ApoE −/− mice. Ann Biomed Eng. Sep.2011 39:2430–44. [PubMed: 21614649]

17. Amirbekian S, Long RC Jr, Consolini MA, Suo J, Willett NJ, Fielden SW, et al. In vivo assessment of blood flow patterns in abdominal aorta of mice with MRI: implications for AAA localization. Am J Physiol Heart Circ Physiol. Oct.2009 297:H1290–5. [PubMed: 19684182]

18. Barisione C, Charnigo R, Howatt DA, Moorleghen JJ, Rateri DL, Daugherty A. Rapid dilation of the abdominal aorta during infusion of angiotensin II detected by noninvasive high-frequency ultrasonography. J Vasc Surg. Aug.2006 44:372–6. [PubMed: 16890871]

19. Klink A, Heynens J, Herranz B, Lobatto ME, Arias T, Sanders HM, et al. In vivo characterization of a new abdominal aortic aneurysm mouse model with conventional and molecular magnetic resonance imaging. J Am Coll Cardiol. Dec 6.2011 58:2522–30. [PubMed: 22133853]

20. Turner GH, Olzinski AR, Bernard RE, Aravindhan K, Karr HW, Mirabile RC, et al. In vivo serial assessment of aortic aneurysm formation in apolipoprotein E-deficient mice via MRI. Circ Cardiovasc Imaging. Nov.2008 1:220–6. [PubMed: 19808546]

21. Goergen CJ, Azuma J, Barr KN, Magdefessel L, Kallop DY, Gogineni A, et al. Influences of aortic motion and curvature on vessel expansion in murine experimental aneurysms. Arterioscler Thromb Vasc Biol. Feb.2011 31:270–9. [PubMed: 21071686]

22. Goergen CJ, Barr KN, Huynh DT, Eastham-Anderson JR, Choi G, Hedehus M, et al. In vivo quantification of murine aortic cyclic strain, motion, and curvature: implications for abdominal aortic aneurysm growth. J Magn Reson Imaging. Oct.2010 32:847–58. [PubMed: 20882615]

23. Ford MD, Black AT, Cao RY, Funk CD, Piomelli U. Hemodynamics of the mouse abdominal aortic aneurysm. J Biomech Eng. Dec.2011 133:121008. [PubMed: 22206425]

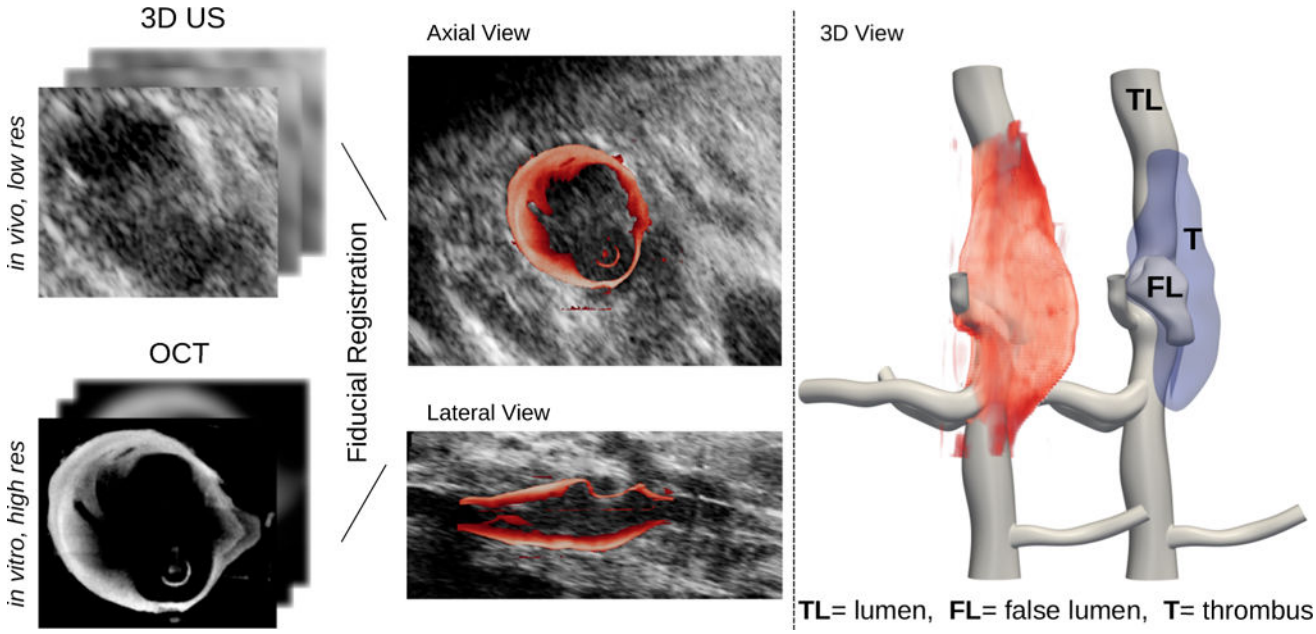

Fig. 1.

Combined 3D US-OCT imaging technique. By co-registering fiducial markers at easily recognizable locations (e.g., branch ostia), we obtained high-resolution merged datasets that provided morphologic detail sufficient to delineate different regions of vasculature in and close to the dissection. Left and middle images show illustrative sections. A reconstructed vessel with a suprarenal dissecting abdominal aortic aneurysm (red), including an enclosed false lumen (FL) and intramural thrombus (T) is shown on the right (blue). res = resolution; US = ultrasound; OCT = optical coherence tomography.

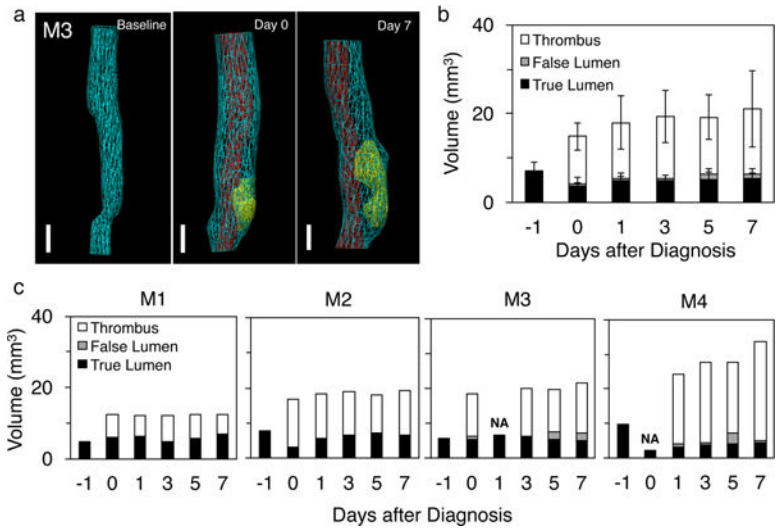

Fig. 2.

Aortic volumes before dissection and during the first week after diagnosis. (a) Representative segmentation results of 3D US images for mouse M3. (b) Average changes in volume across different regions within each of the four lesions (M1 to M4). (c) Volume changes over time for all four mice studied (M1 to M4). Total volume of the lesion includes true lumen, false lumen, and thrombus; volume for the dissected region includes false lumen and thrombus. A thickened vessel wall without thrombus is present in M1. NA = no measurement made due to interference from bowel gas in US images (see image of M4 in Fig. 6).

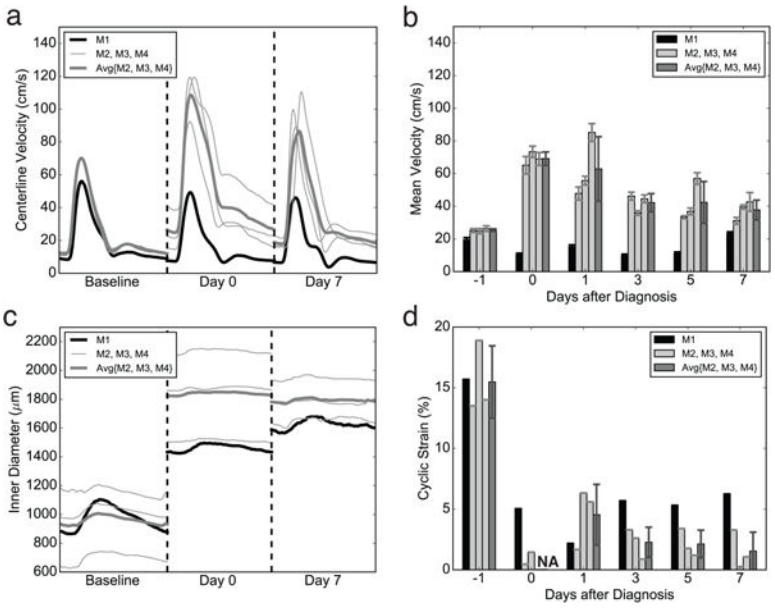

Fig. 3.

Evolution of average velocity and wall displacement waveforms as assessed by US measurements before and during the first week after diagnosis. (a) True lumen centerline velocity waveforms were averaged over 20 or more cardiac cycles. Measurements were acquired just proximal to the location of the orifice of the dissection at baseline (day -1), at diagnosis (day 0), and one week after diagnosis (day 7). (b) Evolution of mean velocity at the same location for all mice during the first week of development. (c) Wall displacement waveforms measured near the point of maximal aortic diameter prior to and after (days 0 and 7) dissection. (d) Evolution of the cyclic circumferential Green strain at the same location for the dissected aneurysmal wall during the first week of development. NA = no measurement made due to interference from bowel gas in US images.

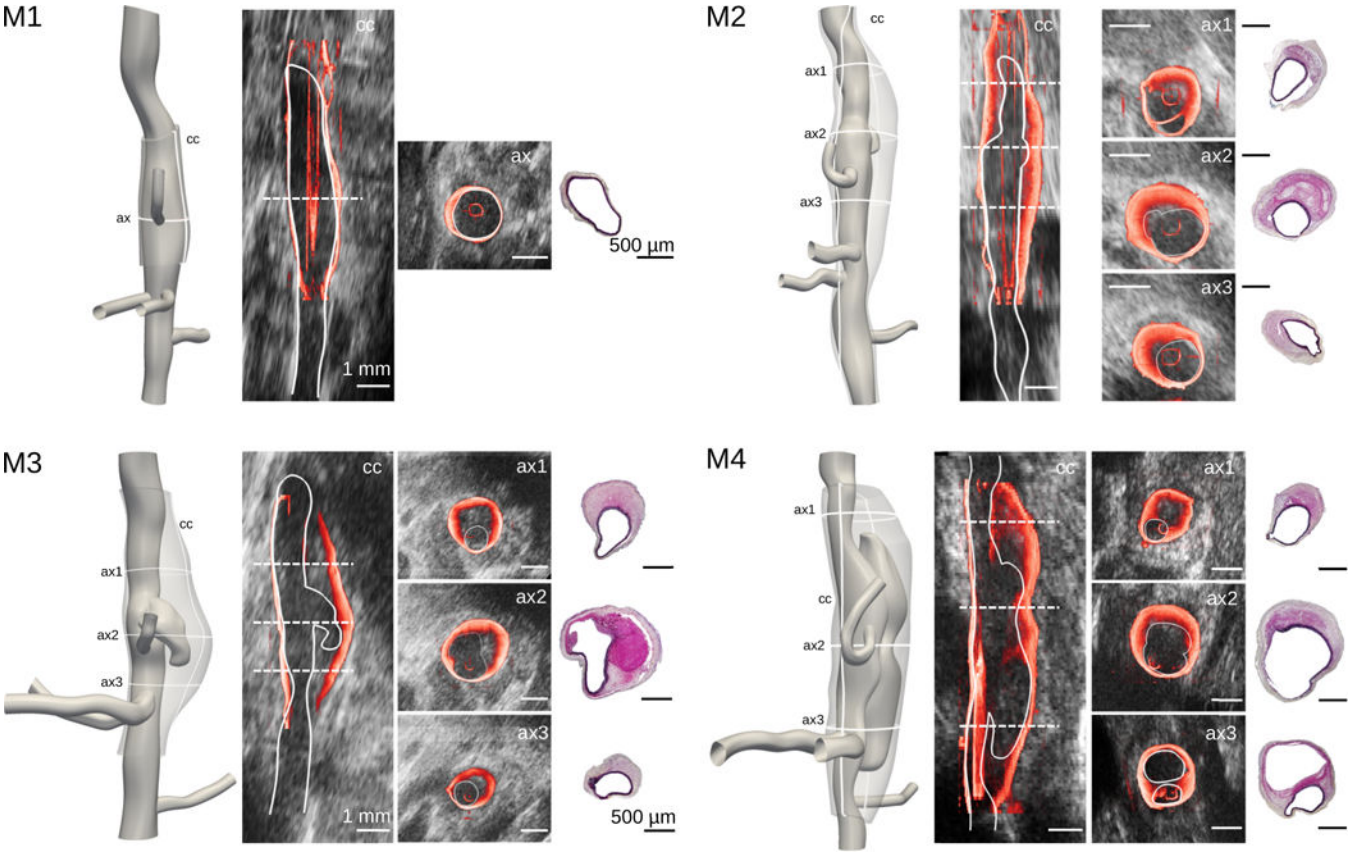

Fig. 4.

3D Solid models reconstructed with our multi-modality technique and compared at key cross-sections. Co-registered 3D US (grey), OCT (red) datasets, and histological sections (Movat stain) taken at approximately the same location are shown. Note that thrombus stains red in Movat, elastin black, and collagen brown-grey. cc – coronal section; ax1- proximal axial cross-section; ax2 – middle axial cross-section, ax3 – distal axial cross-section, ax – representative axial cross-section for M1, which exhibited little axial variation. Note that the cannula used in the OCT studies is visualized in part in the cross-sectional views (inner red circle). White scale bar = 1 mm; black scale bar = 500 μm. Recall Fig. 1 where OCT and US images are shown separately for the same sections.

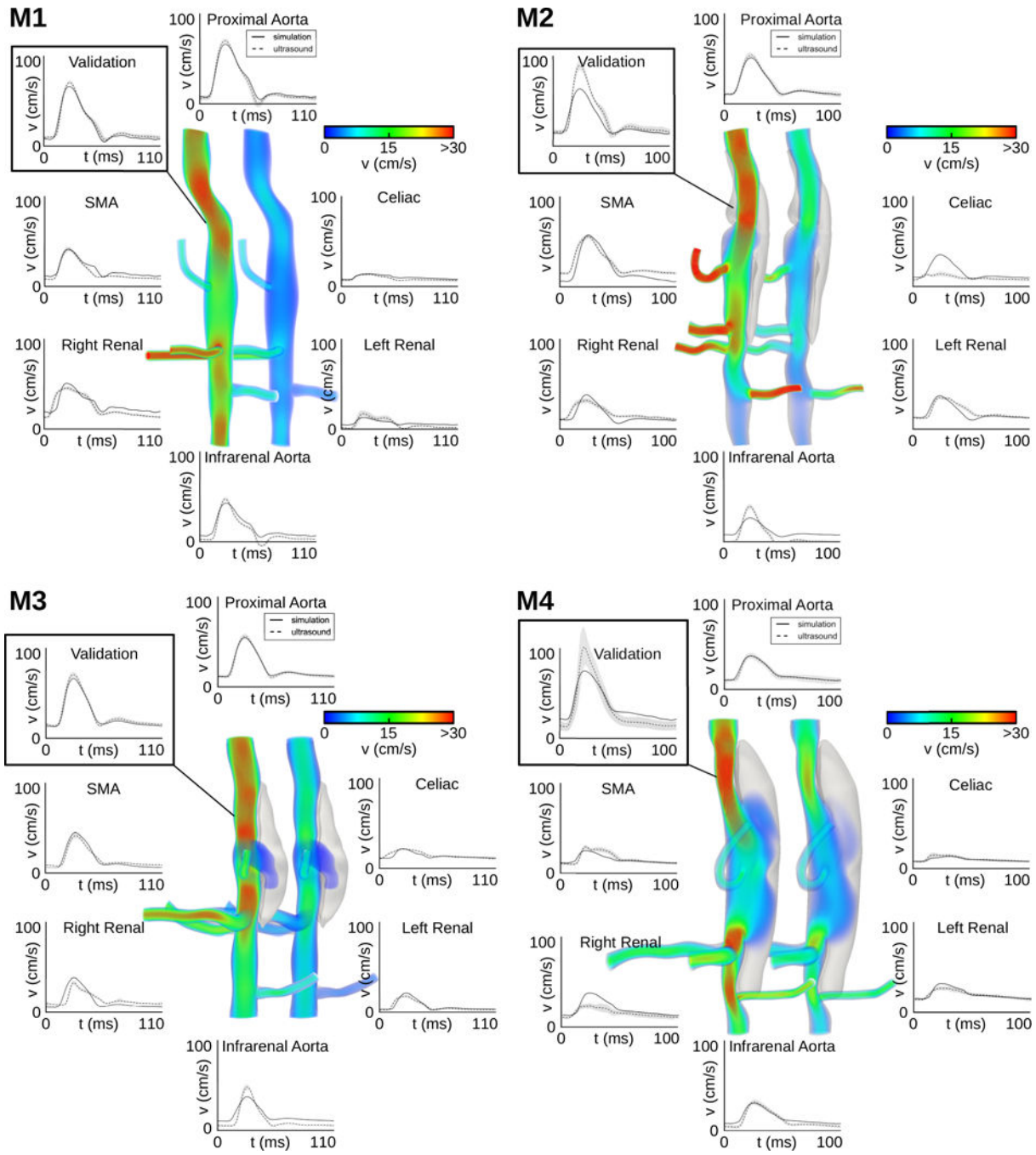

Fig. 5.

Volume rendering and mean velocity waveforms for computational simulations for mice M1 to M4. Color-coded simulations display the velocity magnitude at systole (left) and diastole (right). Simulated velocity waveforms (solid lines) are also compared to ultrasound measurements (dashed lines) at all major inlets and outlets as well as at an intermediate proximal location used to validate, and not inform, the model.

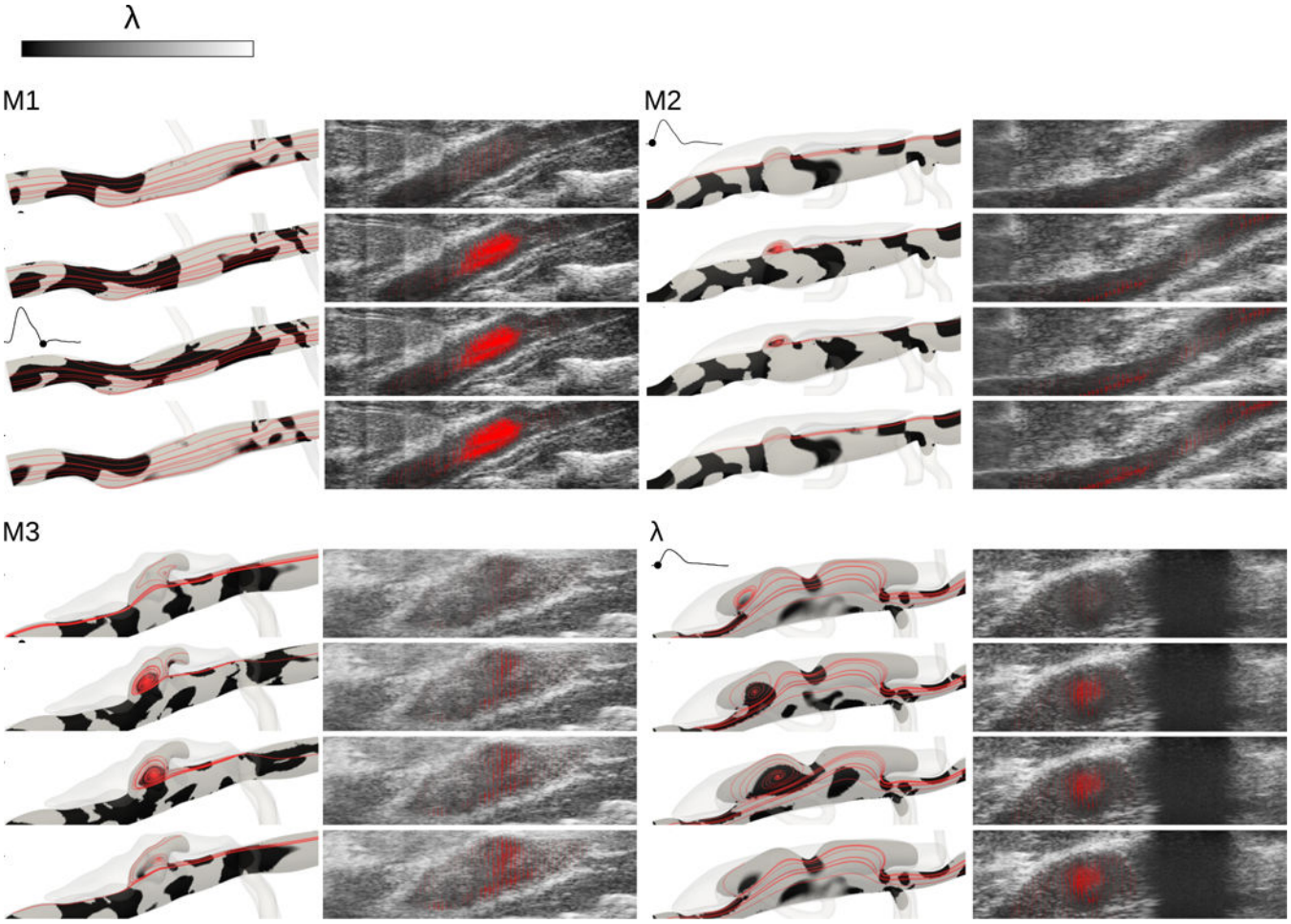

Fig. 6.

Comparison of hemodynamic simulations with EKV snapshots for mice M1 to M4. Color-coded λ_2 distributions in lateral cross-sections (left) show evolving vortical structures throughout a cardiac cycle. Overlapped in red are selected streamlines (tangents to computed velocities). EKV snapshots (right) are overlapped to representative trajectories tracked using a digital image correlation algorithm. The white asterisk denotes a region of bowel gas obstruction.

TABLE I

COMPARISON OF LENGTH AND VOLUME MEASUREMENTS OBTAINED USING 3D US IMAGES ALONE VERSUS ENRICHED 3D US+OCT IMAGES.

Mouse	Technique	Length (mm)	Volume/Length (mm^2)				
			True Lumen	Total Lesion	Dissection	False Lumen	Thrombus[a]
M1	US	6.8	1.0	1.82	0.77	0	0.77[a]
	US+OCT	3.8	0.99	2.14	1.14	0	1.14[a]
M2	US	9.5	0.69	2.01	1.33	0	1.33
	US+OCT	8.4	0.74	2.06	1.31	0.01	1.30
M3	US	8.3	0.61	2.62	2.02	0.26	1.75
	US+OCT	7.8	0.66	2.76	2.09	0.17	1.92
M4	US	10.5	0.43	3.22	2.79	0.05	2.74
	US+OCT	8.6	0.71	3.58	2.87	0.88	1.99

All volume measurements (5 rightmost columns) are normalized by the corresponding lesion length because part of the sample was excluded via tissue cleaning and cannulation prior to OCT imaging. True Lumen = volume of the aorta normalized by length, Total lesion = volume of the whole visible lesion, including true lumen, false lumen, thrombus, and wall thickness, Dissection = Total lesion – True Lumen, False Lumen = blood filled volume of the intramural cavity, Thrombus = Dissection – False Lumen.

[a]Note that M1 did not present either a true dissection or an intramural thrombus and therefore volume measurements refer to the thickened vessel wall.

TABLE II

INLET AND OUTLET BOUNDARY CONDITIONS USED IN THE FLUID DYNAMIC SIMULATIONS.

	Proximal Aorta	Celiac		SMA		Right Renal		Left Renal		Infrarenal	
	Q	R_T ($\times 10^3$)	C ($\times 10^{-6}$)	R_T ($\times 10^3$)	C ($\times 10^{-6}$)	R_T ($\times 10^3$)	C ($\times 10^{-6}$)	R_T ($\times 10^3$)	C ($\times 10^{-6}$)	R_T ($\times 10^3$)	C ($\times 10^{-6}$)
M1	87.6	4.84	1.00	2.08	28.9	1.13	33.1	3.90	8.68	0.544	201
M2	65.2	2.60	6.39	1.03	266	1.25	120	1.54	119	1.17	393
M3	110.4	2.37	13.7	0.734	299	1.59	111	4.49	31.7	0.338	99.6
M4	71.6	3.27	3.79	0.763	78.2	1.02	25.1	1.73	29.3	0.633	196

SMA = superior mesenteric artery, Q = average inlet flow rate ($mm^3\ s^{-1}$), R_T = terminal resistance ($g\ mm^{-4}\ s^{-1}$), C = capacitance ($g^{-1}\ mm^4\ s^2$).

TABLE III

CHARACTERISTIC FEATURES OF THE FOUR LESIONS STUDIED (M1 TO M4), ORDERED BASED ON THE SIZE OF THE FALSE LUMEN AT DAY 7 FOLLOWING THE ONSET OF THE DISSECTION.

Spectrum of lesion characteristics		M1	M2	M3	M4
Morphologic description at day 7	Daugherty's classification (Type I, II, III or IV)	I	II	III	III
	Presence and size of false lumen	−	+ small	+	+ large
	Presence of thrombus	−	+	+	+
Volumetric thrombus growth between days 0 and 7	% change in thrombus volume	0%	15%	12%	20%
	% change in thrombus length	0%	3%	2%	5%
General Information	P (mmHg)[a]	160	140	145	120
	HR (bpm)	566	601	539	636
Average hemodynamic indices in aorta / dissection	Δv at stenosis	−26%	27%	45%	45%
	TAWSS (Pa)	−	0.60	0.22	0.56
	OSI	−	0.11	0.20	0.14

Type I = Dilated lumen without thrombus, Type II = Remodeled tissue containing thrombus, Type III = Bulbous remodeled tissue containing thrombus, Type IV = Multiple dilations containing thrombus, TAWSS = time-averaged wall shear stress, OSI = oscillatory shear index.

[a]Systolic blood pressures measured at day 7 post-surgery. Supplemental Fig. IV shows a complete set of blood pressure measurements